# Optimal 3D Highly Anisotropic Mesh Adaptation Based on the Continuous Mesh Framework

Adrien Loseille[1,2] and Frédéric Alauzet[2]

[1] CFD Center, Dept. of Computational and Data Sciences, College of Science, MS 6A2, George Mason University, Fairfax, VA 22030-4444, USA
aloseill@gmu.edu

[2] INRIA Paris-Rocquencourt, Projet Gamma, Domaine de Voluceau, BP 105, 78153 Le Chesnay cedex, France
Frederic.alauzet@inria.fr

**Abstract.** This paper addresses classical issues that arise when applying anisotropic mesh adaptation to real-life 3D problems as the loss of anisotropy or the necessity to truncate the minimal size when discontinuities are present in the solution. These problematics are due to the complex interaction between the components involved in the adaptive loop: the flow solver, the error estimate and the mesh generator. A solution based on a new continuous mesh framework is proposed to overcome these issues. We show that using this strategy allows an optimal level of anisotropy to be reached and thus enjoy the full benefit of unstructured anisotropic mesh adaptation: optimal distribution of the degrees of freedom, improvement of the ratio accuracy with respect to cpu time, ...

**Keywords:** Anisotropy; multi-scale mesh adaptation; metric-based mesh adaptation; continuous mesh; convergence order; Euler equations.

## Introduction

Nowadays, there is no more need to recall the benefits of metric-based mesh adaptation when dealing with anisotropic physical phenomena. A lot of 3D successful examples on real-life problems have already proved its efficiency [3, 6, 11, 18, 19]. However, one question remains: are the adaptive computations really anisotropic or optimal? Apart from its simplicity, this question raises, as we will see, many other capital issues: assessment of the numerical solution, convergence of the computation at the theoretical order, automatic detection and capturing of all the scales of the solution, ... Consequently, answering positively to these questions is not straightforward as we face both theoretical and practical difficulties. Indeed, claiming that a mesh is optimal requires at least the definition of a proper cost function along with the possibility of differentiating it. A classical cost function is the interpolation error. However, problems occur when attempting to differentiate it with respect to a discrete mesh in order to derive the optimal one. Indeed, the differentiation

is not defined on the space of discrete meshes. Despite this weakness, if we now assume that a specification of the optimal can be exhibited, it is of main importance to derive a numerical algorithm to generate it practically. Being able to guarantee the convergence of the algorithm to the optimal continuous solution is a supplementary difficulty.

We first recall the formulation of the mesh adaptation problem for minimizing the interpolation error. The problematics arising when the function becomes a numerical solution are then illustrated on a simple example.

*An initial ill-posed problem.* In its more general form, the problem of mesh adaptation consists in finding the mesh $\mathcal{H}$ of $\Omega$ that minimizes a given error for a given function $u$. For the sake of simplicity, we consider here the linear interpolation error $u - \Pi_h u$ controlled in $\mathbf{L}^p$ norm. Note that considering other norms works as well [13]. The problem is thus stated in an *a priori* way:

$$\text{Find } \mathcal{H}_{opt} \text{ having } N \text{ nodes such that } E(\mathcal{H}_{opt}) = \min_{\mathcal{H}} \|u - \Pi_h u\|_{\mathbf{L}^p(\Omega)} \,. \quad (1)$$

As it, Problem (1) is a global combinatorial problem which turns out to be intractable practically. Indeed, both topology and vertices location need to be optimized. Consequently, simpler problems are considered to approximate the solution. A common simplification is to perform a **local analysis** of the error instead of considering the global problem. A first set of methods consists in deriving the optimal element shape [2]. A second set consists in deriving a local bound of the interpolation error. This bound is then transformed into a metric-based estimate [8, 9, 13]. Direct minimization of the error can be also considered by using the interpolation error as a cost function directly in the mesh generator [14]. All these strategies have in common the resolution of a local problem as they act in the vicinity of an element. Consequently, such error minimizations are equivalent to a steepest descent algorithm that converges only to a **local minimum** with poor convergence properties. This drawback arises because of considering directly the **minimization on a discrete mesh**.

*Loss of anisotropy when turning to numerical solutions.* When the solution $u$ becomes a numerical solution $u_h$ provided by a solver, additional problematics arise in the resolution of Problem (1). The choice of the error estimate used to derive the metric becomes of main importance. To illustrate this point, we consider a standard metric-based error estimate as in [4], *i.e.,* the control of the interpolation error in $\mathbf{L}^\infty$ norm, for the accurate capturing of shock-waves inside a scramjet. This is done by considering a recovered Hessian of one variable of the flow field (mach, pressure, ...). The final result is shown in Figure 1. If the final adapted mesh seems perfectly anisotropic (left), a closer view around a shock reveals a complete loss of the anisotropy (right). A second problem is that such a strategy does not capture the small-scale features of the flow. Several modifications of this Hessian-based estimate

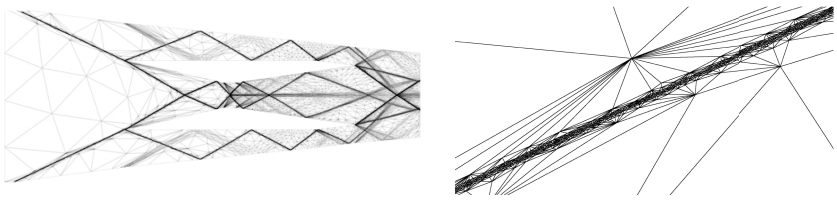

**Fig. 1.** Scramjet adaptive computation based on a control of the interpolation error in $\mathbf{L}^\infty$ norm

have been considered to overcome this issue. For instance, the following local normalizations:

$$\frac{|H|}{|u|}, \frac{|H|}{|u| + h\,\|\nabla u\|_2}, \frac{|H|}{\gamma|u| + (1-\gamma)h\|\nabla u\|_2}, \tag{2}$$

were introduced in [4, 15, 9], respectively, as an attempt to capture all the scales of the solution. However, the control of the interpolation error remains in $\mathbf{L}^\infty$ norm. If more scales of the solution are captured, the **loss of anisotropy** remains and the request for a **minimal size** prescription is still **necessary**.

*Continuous mesh framework and multi-scale mesh adaptation.* To overcome the previous issues, a complete duality between discrete entities and continuous ones is introduced using classical concepts of Differential Geometry as Riemannian metric space. In the proposed continuous framework, notions of continuous mesh, continuous element and continuous interpolation operator naturally appear. This discrete-continuous duality is demonstrated from equivalence formula. In this framework, Problem (1) can be recast as a continuous optimization problem. Contrary to discrete-based study, the continuous formulation succeeds in solving **globally** the optimal interpolation error problem by using powerful mathematical tools as the calculus of variations. When dealing with numerical simulations, the use of $\mathbf{L}^p$ norm interpolation error control enables us to **capture all the scales** of the numerical solution. Numerical experiments show that solution scales that have an amplitude 1 000 times lower than the largest one are still captured and refined. From a practical point of view, prescribing a **minimal size is no more required**. This results in the generation of highly anisotropic meshes. Moreover, the analysis for regular functions predicts a second order convergence for the mesh adaptation algorithm. We show that this order is preserved on numerical solutions even when they are issued from flows with shocks with a modern high-order shock capturing solver. Verifying numerically this second order of convergence is a first assessment of computations.

*Outline.* The main results associated with the continuous mesh framework are reviewed in Section 1. Section 2 deals with the discrete and continuous

equivalence for the local interpolation error. Then, the optimal continuous mesh minimizing the global interpolation error in $\mathbf{L}^p$ norm is derived in Section 3. Practical implementation of the continuous mesh framework and theory assessment on complex numerical simulations are done in Section 4.

## 1 Continuous Mesh Framework

All the notions are introduced in 3D even if all the concepts extend to $n$D as well. Most of the time the complete proofs are skipped for conciseness purposes. However, they are all available in [16, 17]. In the following, a metric tensor $\mathcal{M}$ is a $3 \times 3$ positive symmetric matrix. When the metric field varies over the domain $\Omega \subset \mathbb{R}^3$, a Riemannian metric space $\mathbf{M} = (\mathcal{M}(\mathbf{x}))_{\mathbf{x}\in\Omega}$ of $\Omega$ is defined. Rewriting locally metric tensor $\mathcal{M}$ gives a new insight of the possibility of metric-based mesh adaptation. In particular, a duality between discrete and continuous views appear clearly. We exemplify in this section the set of meshes that are represented by Riemannian metric space $\mathbf{M}$. The study is first done locally for an element and then generalized to the whole computational domain $\Omega$. These considerations are based on the concept of unit mesh [10], recalled hereafter.

*Local duality.* An element $K$ (a tetrahedron in 3D) is **unit** with respect to a constant metric tensor $\mathcal{M}$ if the length of all its edges is unit in metric $\mathcal{M}$. If $K$ is given by its list of edges $(\mathbf{e_i})_{i=1..6}$, then :

$$\forall i = 1, ..., 6, \;\; \ell_{\mathcal{M}}(\mathbf{e_i}) = 1 \text{ with } \ell_{\mathcal{M}}(\mathbf{e_i}) = \sqrt{{}^t\mathbf{e_i}\,\mathcal{M}\,\mathbf{e_i}}.$$

If $K$ is composed only of unit length edges then its volume $|K|_{\mathcal{M}}$ in $\mathcal{M}$ is constant equal to:

$$|K|_{\mathcal{M}} = \frac{\sqrt{2}}{12} \;\text{ and }\; |K| = \frac{\sqrt{2}}{12}(\det(\mathcal{M}))^{-\frac{1}{2}},$$

where $|K|$ is its Euclidean volume. The function *unit with respect to* defines classes of equivalences of discrete elements.

**Proposition 1 (Equivalence classes).** *Let $\mathcal{M}$ be a constant metric tensor, there exists a non-empty infinite set of unit elements with respect to $\mathcal{M}$. Conversely, given an element $K = (\mathbf{e_i})_{i=1..6}$ such that $|K| \neq 0$, then there is a unique metric tensor $\mathcal{M}$ for which element $K$ is unit with respect to $\mathcal{M}$.*

The previous proposition induces deeper relationships between $\mathcal{M}$ and the set of unit discrete elements. These relations write as geometric invariants [16].

**Proposition 2 (Geometric invariant).** *Let $\mathcal{M}$ be a constant metric tensor and $K$ be a unit element with respect to $\mathcal{M}$. We denote by $(\mathbf{e}_i)_i$ its edges list. Then, the following invariant holds for all symmetric matrix $H$:*

$$\sum_{i=1}^{6} {}^t\mathbf{e}_i\, H\mathbf{e}_i = 2\,\mathrm{trace}(\mathcal{M}^{-\frac{1}{2}} H \mathcal{M}^{-\frac{1}{2}})\,. \tag{3}$$

*Global duality.* When dealing with a Riemannian metric space $\mathbf{M} = (\mathcal{M}(\mathbf{x}))_{\mathbf{x}\in\Omega}$, the main complexity is to take into account the variations of the function $\mathbf{x} \mapsto \mathcal{M}(\mathbf{x})$. To simplify the analysis, $\mathbf{M}$ is first rewritten in order to distinguish local properties from global ones.

**Proposition 3.** *A Riemannian metric space* $\mathbf{M} = (\mathcal{M}(\mathbf{x}))_{\mathbf{x}\in\mathbf{\Omega}}$ *locally writes:*

$$\forall \mathbf{x} \in \Omega, \quad \mathcal{M}(\mathbf{x}) = d^{\frac{2}{3}}(\mathbf{x})\,\mathcal{R}(\mathbf{x}) \begin{pmatrix} r_1^{-\frac{2}{3}}(\mathbf{x}) & & \\ & r_2^{-\frac{2}{3}}(\mathbf{x}) & \\ & & r_3^{-\frac{2}{3}}(\mathbf{x}) \end{pmatrix} {}^t\mathcal{R}(\mathbf{x}),$$

*where*

- *the density $d$ is equal to: $d = (h_1h_2h_3)^{-1} = (\lambda_1\lambda_2\lambda_3)^{\frac{1}{2}}$, with $\lambda_i$ the eigenvalues of $\mathcal{M}$ and $h_i = \lambda_i^{-\frac{1}{2}}$*
- *the anisotropic quotients $r_i$ are equal to: $r_i = h_i^3\,(h_1h_2h_3)^{-1}$*
- *$\mathcal{R}$ is the eigenvectors matrix of $\mathcal{M}$.*

The anisotropy is given by the anisotropic quotients, the level of accuracy is given by the density and the orientation by the orthonormal matrix $\mathcal{R}$. Global properties of $\mathbf{M}$ can be deduced by integrating these local quantities on $\Omega$. When integrating $d$ over $\Omega$, the complexity of $\mathbf{M}$ is defined:

$$\mathcal{C}(\mathbf{M}) = \int_\Omega d(\mathbf{x})\,d\mathbf{x} = \int_\Omega \sqrt{\det(\mathcal{M}(\mathbf{x}))}\,d\mathbf{x}.$$

This quantity can be viewed as the continuous counterpart of the number of vertices of a mesh. In the context of error estimation, this notion enables the study of the order of convergence with respect to a sequence of Riemannian metric spaces having an increasing complexity. Consequently, the complexity $\mathcal{C}(\mathbf{M})$ is also the continuous counterpart of the classical parameter $h$ used for uniform meshes while studying convergence order.

The set of discrete meshes represented by $\mathbf{M}$ is more complex to describe than the class of unit elements. The problem arises from the impossibility to tessellate $\mathbb{R}^3$ uniquely with the regular tetrahedron, see discussions in [17]. Consequently, the notion of unit element does not extend as well to a mesh. In order to ensure existence, the notion of quasi-unit element is devised. This definition takes into account the variations of the continuous mesh:

**Definition 1 (Quasi-unit element).** *A tetrahedron $K$ defined by its list of edges $(\mathbf{e_i})_{i=1\ldots6}$ is said quasi-unit for $\mathcal{M}$ if*

$$\forall i \in [1,6], \quad \ell_{\mathcal{M}}(\mathbf{e_i}) \in \left[\frac{1}{\sqrt{2}}, \sqrt{2}\right] \quad \textit{and} \quad Q_{\mathcal{M}}(K) \in [\alpha, 1] \quad \textit{with} \quad \alpha > 0\,, \tag{4}$$

*where*

$$Q_{\mathcal{M}}(K) = \frac{36}{3^{\frac{1}{3}}} \frac{|K|_{\mathcal{M}}^{\frac{2}{3}}}{\sum_{i=1}^{6} \ell_{\mathcal{M}}^2(\mathbf{e}_i)} \in [0,1], \quad \textit{with } |K|_{\mathcal{M}} = \int_K \sqrt{\det(\mathcal{M}(\mathbf{x}))}\, \mathrm{d}\mathbf{x},$$
$$\textit{and } \ell_{\mathcal{M}}(\mathbf{e}_i) = \int_0^1 \sqrt{{}^t\mathbf{ab}\, \mathcal{M}(\mathbf{a} + t\,\mathbf{ab})\, \mathbf{ab}}\, \mathrm{d}t, \quad \textit{with } \mathbf{e}_i = \mathbf{ab}. \tag{5}$$

The quality function $Q_{\mathcal{M}}$ ensures that the volume and the shape of the elements are controlled while generating elements with quasi-unit edges lengths. The integral in the computation of $\ell_{\mathcal{M}}$ given by (5) is necessary to take into account the variations of $\mathbf{M}$ along each edge $\mathbf{e}_i$. A discrete mesh is **unit** with respect to $\mathbf{M}$ when it is only composed of quasi-unit elements.

Propositions 1 and 3 highlights a duality between discrete entities and continuous ones. It results that, in the proposed continuous framework, a metric tensor $\mathcal{M}$ is assimilated to a continuous element and a **continuous mesh** of a domain $\Omega$ is defined by a collection of continuous elements $\mathbf{M} = (\mathcal{M}(\mathbf{x}))_{\mathbf{x}\in\Omega}$, *i.e.,* a Riemannian metric space. In particular, for an element, this duality is justified by strict analogy between discrete and continuous notions: orientation vs. matrix $\mathcal{R}$, stretching vs. $r_i$ and size vs. $d$. For a mesh, we point out the duality between the number of vertices and $\mathcal{C}(\mathbf{M})$. Proposition 2 also illustrates a duality between geometric quantities. This duality will be even reinforced in the next section by studying the interpolation error.

In what follows, the continuous terminology is employed to emphasize the exhibited duality.

## 2 Interpolation Error: Discrete-Continuous Duality

As our intent is to propose a fully discrete-continuous duality, it is not enough to derive only the optimal mesh arising from an interpolation error bound as in classical studies on interpolation error [4, 9, 13]. Instead, we want to evaluate the interpolation error for any functions on any continuous meshes without imposing some optimality conditions as alignment, equi-distribution, ... We show in this section that the interpolation error can be computed analytically for a given function on a given continuous mesh. We start with an estimate for quadratic functions. The general case is deduced from this study.

*An error estimate for quadratic functions.* In this section, we consider a quadratic function $u$ defined on a domain $\Omega \subset \mathbb{R}^3$. The function is given by its matrix representation:

$$\forall \mathbf{x} \in \Omega, \quad u(\mathbf{x}) = \frac{1}{2}\, {}^t\mathbf{x}\, H\, \mathbf{x},$$

where $H$ is a symmetric matrix representing the Hessian of $u$. For every symmetric matrix $H$, $|H|$ denotes the positive symmetric matrix deduced from

$H$ by taking the absolute values of its eigenvalues. The function $u$ is linearly interpolated on a tetrahedron $K$. We denote by $\Pi_h u$ the linear interpolate of $u$ on $K$. We can now state the following result:

**Proposition 4.** *For every quadratic function $u$, its linear interpolation error in $\mathbf{L}^1$ norm on a tetrahedron $K$ verifies:*

$$\|u - \Pi_h u\|_{\mathbf{L}^1(K)} \leq \frac{|K|}{40} \sum_{i=1}^{6} {}^t\mathbf{e}_i |H| \mathbf{e}_i,$$

*where $(\mathbf{e}_i)_{i=1,6}$ is the set of edges of $K$.*

*The previous inequality becomes an equality when $u$ is elliptic or parabolic.*

If $K$ is now assumed to be unit with respect to $\mathcal{M}$, the following theorem holds:

**Theorem 1.** *For all unit elements $K$ with respect to $\mathcal{M}$, the interpolation error of $u$ in $\mathbf{L}^1$ norm does not depend on the element shape and is only a function of the Hessian $H$ of $u$ and of $\mathcal{M}$. In 3D, for all unit tetrahedra $K$ in $\mathcal{M}$, the following equality holds:*

$$\|u - \Pi_h u\|_{\mathbf{L}^1(K)} = \frac{\sqrt{2}}{240} \det(\mathcal{M}^{-\frac{1}{2}}) \operatorname{trace}(\mathcal{M}^{-\frac{1}{2}} H \mathcal{M}^{-\frac{1}{2}}). \tag{6}$$

It is important to note that Relation (6) links an infinite set of elements (on the left-hand side) to a unique entity: $\mathcal{M}$ (on the right-hand side). Moreover, it shows that whatever the choice of unit-element made by the mesh generator, the resulting interpolation error is always the same as it is only function of metric $\mathcal{M}$. Consequently, this theorem demonstrates the possibility to evaluate the interpolation error for continuous element $\mathcal{M}$ associated with discrete element $K$. When $u$ is no more quadratic and when the interpolation error is computed on a continuous mesh $\mathbf{M}$, the following continuous discrete local equivalence is proved:

**Theorem 2 (Discrete-continuous duality).** *Let $u$ be a twice continuously differentiable fonction of a domain $\Omega$ and $(\mathcal{M}(\mathbf{x}))_{\mathbf{x}\in\Omega}$ be a continuous mesh of $\Omega$. Then, there exists a unique function $\pi_{\mathcal{M}}$ such that:*

$$\forall \mathbf{a} \in \Omega\,, \quad |u - \pi_{\mathcal{M}} u|(\mathbf{a}) = 2\,\frac{\|u_Q - \Pi_h u_Q\|_{\mathbf{L}^1(K)}}{|K|},$$

*for every $K$ unit element with respect to $\mathcal{M}(\mathbf{a})$ and where $u_Q$ is the quadratic model of $u$ at $\mathbf{a}$.*

This theorem underlines another discrete-continuous duality by pointing out a continuous counterpart of the interpolation error. For this reason, we propose the following formalism: $\pi_{\mathcal{M}}$ is called continuous linear interpolate and $|u - \pi_{\mathcal{M}} u|$ represents the continuous dual of the interpolation error. The continuous linear interpolate is defined by:

$$\pi_{\mathcal{M}} u(\mathbf{a}) = u(\mathbf{a}) + \nabla u(\mathbf{a}) + \frac{1}{c_n} \mathrm{trace}(\mathcal{M}^{-\frac{1}{2}}(\mathbf{a})\, H(\mathbf{a})\, \mathcal{M}^{-\frac{1}{2}}(\mathbf{a})),$$

where $c_n$ is 1/8 in 2D and 1/10 in 3D [17]. This result allows us to compute interpolation errors analytically. The following examples give a comparison between continuous and discrete interpolation errors evaluation.

*Continuous examples.* The set of 2D continuous meshes $\mathbf{M}(\alpha) = (\mathcal{M}_\alpha(\mathbf{x}))_{\mathbf{x}\in\Omega}$ is defined on the square domain $\Omega = [0,1] \times [0,1]$ by:

$$\mathcal{M}_\alpha(x,y) = \alpha \begin{pmatrix} h_1^{-2}(x,y) & 0 \\ 0 & h_2^{-2}(x,y) \end{pmatrix},$$

where $h_1(x,y) = 0.1(x+1) + 0.05(x-1)$ and $h_2(x,y) = 0.2$. The parameter $\alpha$ is used to control the level of accuracy of the mesh. The continuous mesh becomes coarser when $\alpha$ decreases but anisotropic quotients and orientations remain constant. This trend is given by the computation of the complexity $\mathcal{C}(\mathbf{M}(\alpha))$:

$$\mathcal{C}(\mathbf{M}(\alpha)) = N(\alpha) = \iint_\Omega \frac{1}{h_1 h_2}(x,y)\,\mathrm{d}x\mathrm{d}y = \frac{200}{3}\ln(2)\alpha.$$

The continuous interpolation error on $\mathbf{M}(\alpha)$ is computed for two analytical functions: $u_1(x,y) = 6x^2 + 2xy + 4y^2$ and $u_2(x,y) = \mathrm{e}^{(2x^2+y)}$. As regards the function $u_1$, the point-wise continuous interpolation error on $\mathbf{M}(\alpha)$ is

$$(u_1 - \pi_{\mathcal{M}} u_1)(x,y) = \frac{27\,x^2 + 18\,x + 35}{800\,\alpha}.$$

The previous expression is then integrated over $\Omega$:

$$\iint_\Omega |u_1 - \pi_{\mathcal{M}} u_1|(x,y)\,\mathrm{d}x\mathrm{d}y = \frac{53}{800\,\alpha} = \frac{53}{21}\frac{\ln(2)}{N(\alpha)}.$$

For the function $u_2$, the point-wise continuous interpolation error on $\mathbf{M}(\alpha)$ is:

$$(u_2 - \pi_{\mathcal{M}} u_2)(x,y) = \frac{e^{4x^2+y}}{8\,\alpha}\left((0.15x + 0.05)^2\,(4 + 16x^2) + 0.05\right).$$

By a direct integration over $\Omega$, it comes:

$$\iint_\Omega |u_2 - \pi_{\mathcal{M}} u_2|(x,y)\,\mathrm{d}x\mathrm{d}y \approx \frac{0.2050950191}{\alpha} \approx \frac{13.673\,\ln(2)}{N(\alpha)}.$$

These analytical evaluations of the continuous interpolation error are compared to the evaluation of the discrete interpolation error on a set of a unit meshes with respect to $\mathbf{M}(\alpha)$ for several values of $\alpha$. These evaluations are plotted in Figure 2 where a perfect correlation is observed. The black-plain lines represent the extremal bound of the interpolation error due to the relaxed notion of quasi-unit elements, cf. Definition 1, while considering uniform

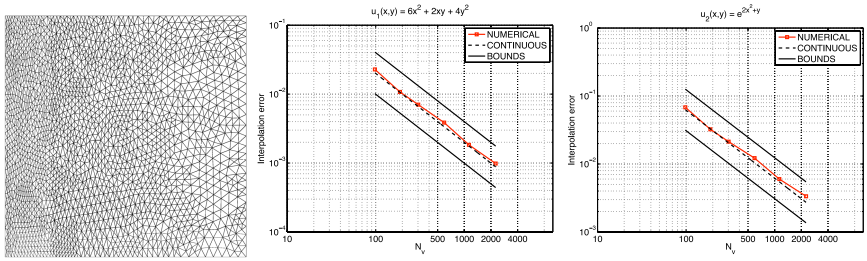


**Fig. 2.** Left, a unit mesh with respect to $\mathbf{M}(\alpha)$ for $\alpha = 32$. Comparison between continuous interpolation error $\|u - \pi_{\mathcal{M}} u\|_{\mathbf{L}^1(\Omega)}$ and discrete interpolation error $\|u - \Pi_h u\|_{\mathbf{L}^1(\Omega)}$ evaluations for the functions $u_1$ (middle) and $u_2$ (right) on $\mathbf{M}(\alpha)$.

meshes in $\mathbf{M}(\alpha)$ with edges length equal to $\sqrt{2}/2$ (lower line) and 2 (upper line).

We now consider the set of 3D continuous meshes $\mathbf{M}(\alpha) = (\mathcal{M}_\alpha(\mathbf{x}))_{\mathbf{x}\in\Omega}$ defined on the domain $\Omega = [0,1] \times [0,1] \times [0,1]$ which are given by:

$$\mathcal{M}_\alpha(x,y,z) = \alpha \begin{pmatrix} h_1^{-2}(x,y,z) & 0 & 0 \\ 0 & h_2^{-2}(x,y,z) & 0 \\ 0 & 0 & h_3^{-2}(x,y,z) \end{pmatrix},$$

$$\text{where} \quad h_1(x,y,z) = 0.1(x+1) + 0.05(x-1),$$
$$h_2(x,y,z) = 0.2 \quad \text{and} \quad h_3(x,y,z) = 0.2(z+2)\,.$$

We consider the interpolation error of the function $u_3(x,y,z) = e^{2x+y+z}$. The continuous linear interpolation error is (see [17] for details):

$$\iiint_\Omega |u_3 - \pi_{\mathcal{M}} u_3|(x,y,z)\,\mathrm{d}x\mathrm{d}y\mathrm{d}z \approx \frac{0.73}{\alpha} \approx \frac{126.215}{N(\alpha)^{\frac{2}{3}}}.$$

Comparisons between continuous and discrete interpolation errors evaluations for the set of continuous meshes are depicted in Figure 3. As previously, the matching between both evaluations is excellent.

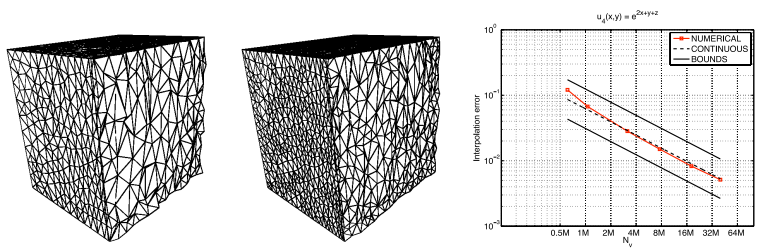


**Fig. 3.** 3D unit meshes with respect to $\mathbf{M}(\alpha)$ for $\alpha = \{16, 32\}$ (left and middle). Right, comparison between continuous interpolation error $\|u_3 - \pi_{\mathcal{M}} u_3\|_{\mathbf{L}^1(\Omega)}$ and discrete interpolation error $\|u_3 - \Pi_h u_3\|_{\mathbf{L}^1(\Omega)}$.

These examples justifies the continuous terminology as the continuous interpolation computation is equivalent to the discrete one. Then, we use this equivalence to derive a global optimal minimizing the continuous interpolation error.

## 3 Optimal Control of the Interpolation Error in $\mathbf{L}^p$ Norm

Using the definition of the linear continuous interpolate $\pi_{\mathcal{M}}$ of Section 2, the following 3D point-wise interpolation error for $u$ on $\mathbf{M} = (\mathcal{M}(\mathbf{x}))_{\mathbf{x}\in\Omega}$ is deduced:

$$e_{\mathcal{M}}(\mathbf{x}) = (u - \pi_{\mathcal{M}} u)(\mathbf{x}) = \frac{1}{10} \sum_{i=1}^{3} h_i^2(\mathbf{x}) |^t\mathbf{v}_i(\mathbf{x})\, H(\mathbf{x})\, \mathbf{v}_i(\mathbf{x})|,$$

where $H$ is the Hessian of $u$, $(\mathbf{v}_i)_{i=1,3}$ the local eigen-directions of $\mathbf{M}$ and $(h_i)_{i=1,3}$ the local sizes of $\mathbf{M}$ along these directions. It is then possible to set the well-posed global optimization problem of finding the optimal continuous mesh minimizing the continuous interpolation error in $\mathbf{L}^p$ norm:

$$\text{Find } \mathbf{M}_{\mathbf{L}^p} = \min_{\mathbf{M}} E_{\mathbf{L}^p}(\mathbf{M}) = \left(\int_\Omega e_{\mathcal{M}}^p\right)^{\frac{1}{p}} = \left(\int_\Omega (u - \pi_{\mathcal{M}} u)^p\right)^{\frac{1}{p}}, \quad (7)$$

under the constraint

$$\mathcal{C}(\mathbf{M}) = \int_\Omega d = N.$$

The constraint on the complexity is added to avoid the trivial solution where all $h_i$ are zero which provides a null error. Contrary to discrete analysis, this problem can be solved globally by using the calculus of variations as it is well-defined on the space of continuous meshes. In [16], it is proved that Problem (7) admits a unique solution. In addition, the following properties hold:

**Theorem 3.** *Let $u$ be a twice continuously differentiable function defined on $\Omega \subset \mathbb{R}^3$, the optimal continuous mesh $\mathbf{M}_{\mathbf{L}^p}(u)$ minimizing Problem (7) reads locally:*

$$\mathcal{M}_{\mathbf{L}^p} = D_{\mathbf{L}^p}\ \det(|H|)^{\frac{-1}{2p+3}}\, |H|, \text{ with } D_{\mathbf{L}^p} = N^{\frac{2}{3}} \left(\int_\Omega \det(|H|)^{\frac{p}{2p+3}}\right)^{-\frac{2}{3}}. \quad (8)$$

*It verifies the following properties:*

- $\mathbf{M}_{\mathbf{L}^p}(u)$ *is unique*
- $\mathbf{M}_{\mathbf{L}^p}(u)$ *is locally aligned with the eigenvectors basis of $H$ and has the same anisotropic quotients as $H$*

- $\mathbf{M}_{\mathbf{L}^p}(u)$ *provides an optimal explicit bound of the interpolation error in* $\mathbf{L}^p$ *norm:*

$$\|u - \pi_{\mathcal{M}_{\mathbf{L}^p}} u\|_{\mathbf{L}^p(\Omega)} = 3\, N^{-\frac{2}{3}} \left( \int_\Omega \det\left(|H|\right)^{\frac{p}{2p+3}} \right)^{\frac{2p+3}{3p}}. \tag{9}$$

- *For a sequence of continuous meshes having an increasing complexity with the same orientation and anisotropic quotients* $(\mathbf{M}^N_{\mathbf{L}^p}(u))_{N=1\ldots\infty}$, *the asymptotic order of convergence verifies:*

$$\|u - \pi_{\mathcal{M}^N_{\mathbf{L}^p}} u\|_{\mathbf{L}^p(\Omega)} \leq \frac{Cst}{N^{2/3}}. \tag{10}$$

*Relation (10) points out a global second order of mesh convergence.*

Note that Bound (9) has been also derived in [5]. However, in our case, all the constants of (9) are explicitly given. In addition, a second order of convergence is predicted. Last but not least, the final difference is that we are able practically to generate a discrete mesh approximating the continuous optimal solution by using any metric-based adaptive mesh generators as soon as the generated meshes verify (5). In addition, this approach is fully compatible with steepest descent methods discussed in the introduction. Indeed, the unit mesh with respect to the global optimal continuous mesh can be used as an initialization, then a discrete steepest descent method can be used to converge toward an optimal discrete mesh.

*Examples.* We first give an example that illustrates why the $\mathbf{L}^\infty$ norm is not well-suited for flow solutions involving different scales. The considered function is:

$$\forall (x,y) \in [0,1]^2, \quad f(x,y) = 0.1 \sin(50x) + \operatorname{atan}\left( \frac{0.1}{\sin(5y) - 2x} \right).$$

It is composed of a main shock induced by the atan function with variations of small amplitudes given by the sine, see Figure 4 (left). Two optimal adapted meshes have been generated: one controlling the $\mathbf{L}^1$ norm and the other controlling the $\mathbf{L}^\infty$ norm of the interpolation error. Both meshes are composed of 100 000 vertices. All the scales are refined with the $\mathbf{L}^1$ norm , see Figure 4 (middle), whereas only the main shock is refined with the $\mathbf{L}^\infty$ norm, see Figure 4 (right).

The second example illustrates the convergence of the adaptive scheme for a 1D discontinuous function, the step function $f_H$, with and without the introduction of an artificial dissipation. Indeed, modern shock capturing schemes that are not compressive generally introduce such dissipation [1]. Figure 5 represents on a uniform mesh the diffused step function $f_h$ on two elements (left) and its linear interpolation $\Pi f_H$ (middle), *i.e.,* its discrete representation without any dissipation. The right picture shows the evolution of the minimal size prescription at each iteration of the mesh adaptation loop for two different error thresholds ($\varepsilon = 0.1$ and $\varepsilon = 0.12$) for both functions. We observed that the

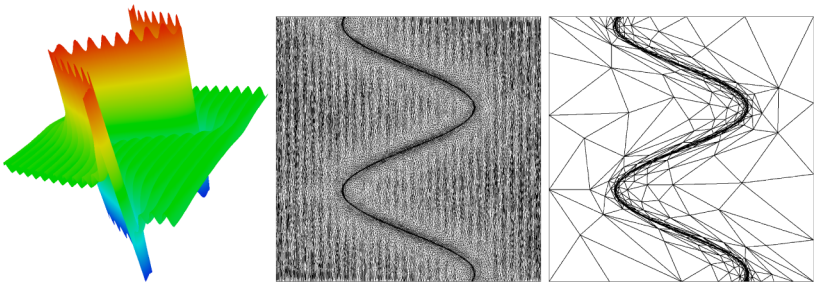

**Fig. 4.** From left to right, iso-values of function $f$, optimal meshes controlling the interpolation error in $\mathbf{L}^1$ norm and in $\mathbf{L}^\infty$ norm

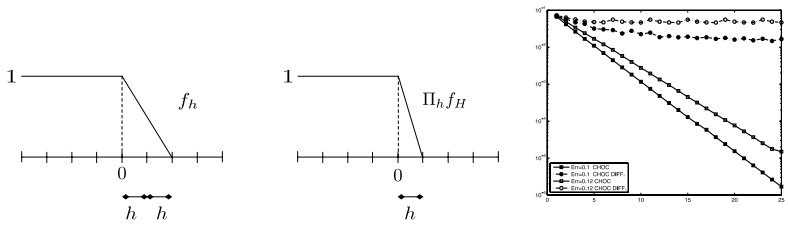


**Fig. 5.** Linear interpolate $\Pi f_H$ of discontinuous function $f_H$ and numerical diffused shock $f_h$. Whatever the level of error $Err$ desired, the minimal size converges when adapting to $f_h$ and diverges when adapting to $f_H$.

minimal size converge progressively towards zero for the step function without any dissipation $f_H$ whereas it converges towards a fixed value for the diffused one $f_h$. Consequently, one may expect that the size in the normal direction to a numerical shock will not tend to zero during the refinement process if a dissipation is introduced. This feature of multi-scale mesh adaptation is verified in Section 4 for a modern shock-capturing scheme.

## 4 3D Numerical Validations

We first review the main modifications that arises when using the previous concept with numerical solutions. This concerns the recovery of derivatives of piecewise linear by element solutions, the adaptive loop and the computation of anisotropic ratios and quotients. Then, several 3D flow simulations involving highly anisotropic meshes are presented. For all the examples, a control of the interpolation error in $\mathbf{L}^2$ norm of the local Mach number is used and **no** minimal size is prescribed.

*High-order approximation and hessian recovery.* In our case, the flow solver provides a continuous piecewise linear by element representation of the solution $u_h$. Consequently, our analysis cannot be applied directly to the numerical solution. The idea is to build a higher order solution approximation $u^*$ of

the exact solution $u$ from $u_h$ which is twice continuously differentiable and to consider $u^*$ in the optimal metric expression (8). Practically, only the Hessian of $u^*$ is recovered [1]. We also mention that the Hessian recovery procedure from discrete data may results in a noisy recovered Hessian. Consequently, using a proper anisotropic mesh gradation is strongly advised to smooth the field of metric tensors.

*A non linear loop.* Anisotropic mesh adaptation is a non-linear problem, therefore, an iterative procedure is required to solve this problem. For stationary simulations, an adaptive computation is carried out *via* a mesh adaptation loop inside which an algorithmic convergence of the mesh-solution couple is sought. At each stage, a numerical solution is computed on the current mesh with the flow solver and is analyzed with a metric-based error estimate providing the optimal metric using (8). Next, an adapted mesh, *i.e.,* a unit mesh, is generated with respect to this metric. The mesh generator used is described in [7]. Finally, the solution is linearly interpolated on the new mesh. This procedure is repeated until convergence of the couple mesh-solution.

*Measuring the anisotropy.* We define some anisotropic measures computation. Anisotropic quotients have been introduced in Section 1 for a continuous element. Deriving this quantity for an element is straightforward. It relies on the fact that there always exists a unique metric tensor for which this element is unit, see Proposition 1. If $\mathcal{M}_K$ denotes the metric tensor associated with element $K$, solving the following linear system provides $\mathcal{M}_K$:

$$(S) \begin{cases} \ell^2_{\mathcal{M}_K}(\mathbf{e}_1) = 1 \\ \vdots \\ \ell^2_{\mathcal{M}_K}(\mathbf{e}_6) = 1\,, \end{cases}$$

where $(\mathbf{e}_i)_{i=1,6}$ is the edges list of $K$ and $\ell^2_{\mathcal{M}_K}(\mathbf{e}_i) = {}^t\mathbf{e}_i\,\mathcal{M}_K\,\mathbf{e}_i$. Note that $(S)$ admits a unique solution as soon as the volume of $K$ is not null. Once $\mathcal{M}_K$ is computed, the anisotropic ratio and the anisotropic quotient are simply given by

$$\text{ratio} = \sqrt{\frac{\min_i \lambda_i}{\max_i \lambda_i}} = \frac{\max_i h_i}{\min_i h_i}, \quad \text{and} \quad \text{quo} = \frac{\max_i h_i^3}{h_1 h_2 h_3},$$

where $(\lambda_i)_{i=1,3}$ are the eigenvalues of $\mathcal{M}_K$ and $(h_i)_{i=1,3}$ are the corresponding sizes. The anisotropic ratio stands for the maximum elongation of a tetrahedron by comparing two eigen-directions. The anisotropic quotient represents the overall anisotropic ratio of a tetrahedron taking into account all the possible directions. It corresponds to the overall gain in three dimensions of **an anisotropic adapted mesh** as compared to **an isotropic adapted mesh**. The gain is of course even larger when compared to a uniform mesh. In the sequel, these measures are used to quantify the obtained level of anisotropy.

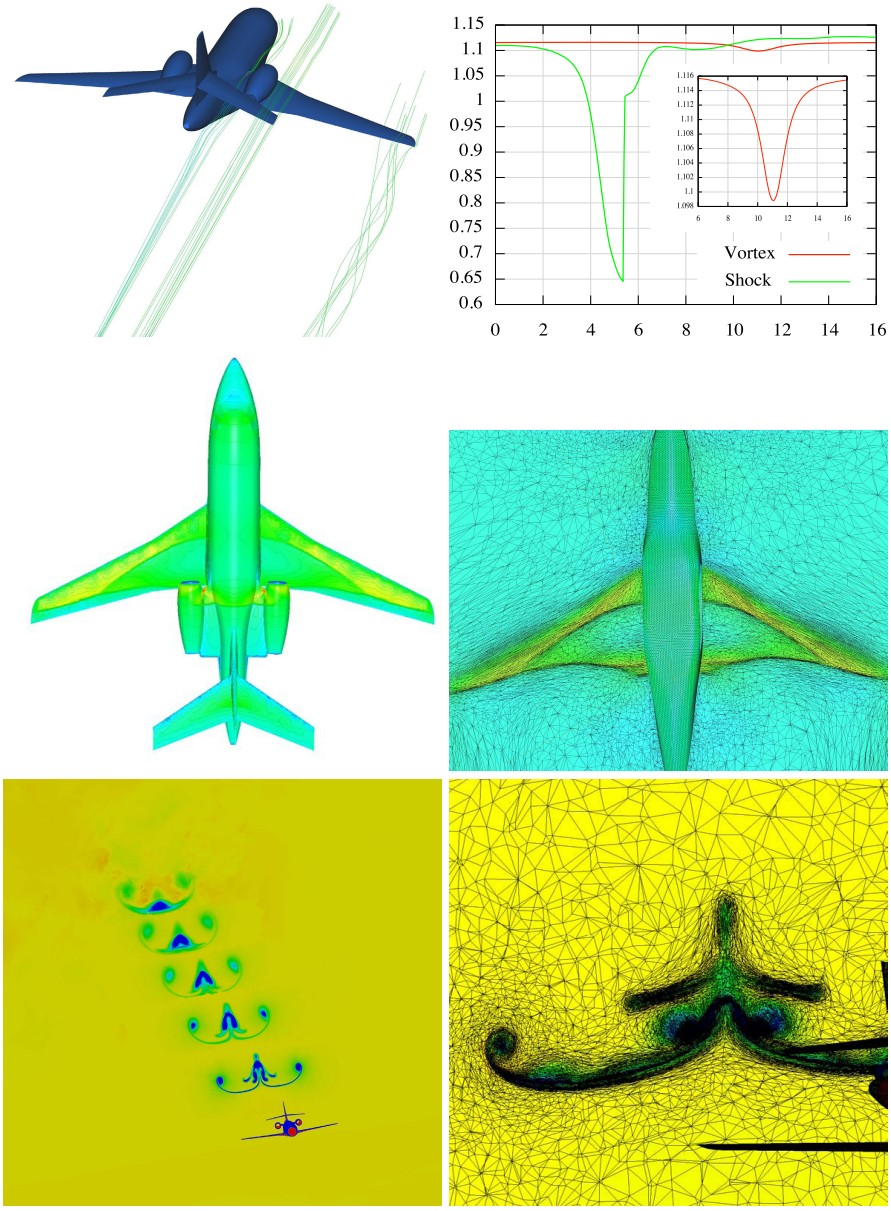


**Fig. 6.** Transonic flow around a Falcon. From top to bottom, from left to right, Falcon geometry along with speed streamlines, difference of amplitudes between the wings shocks and the tip vortices, Mach iso-values on the aircraft, cut in the volume mesh that shows how the wings shocks are captured, Mach iso-values in planes located at 100, 200, 300, 400 and 500 meters behind the Falcon and a cut in the final volume mesh behind the Falcon showing how vortices are captured in the mesh.

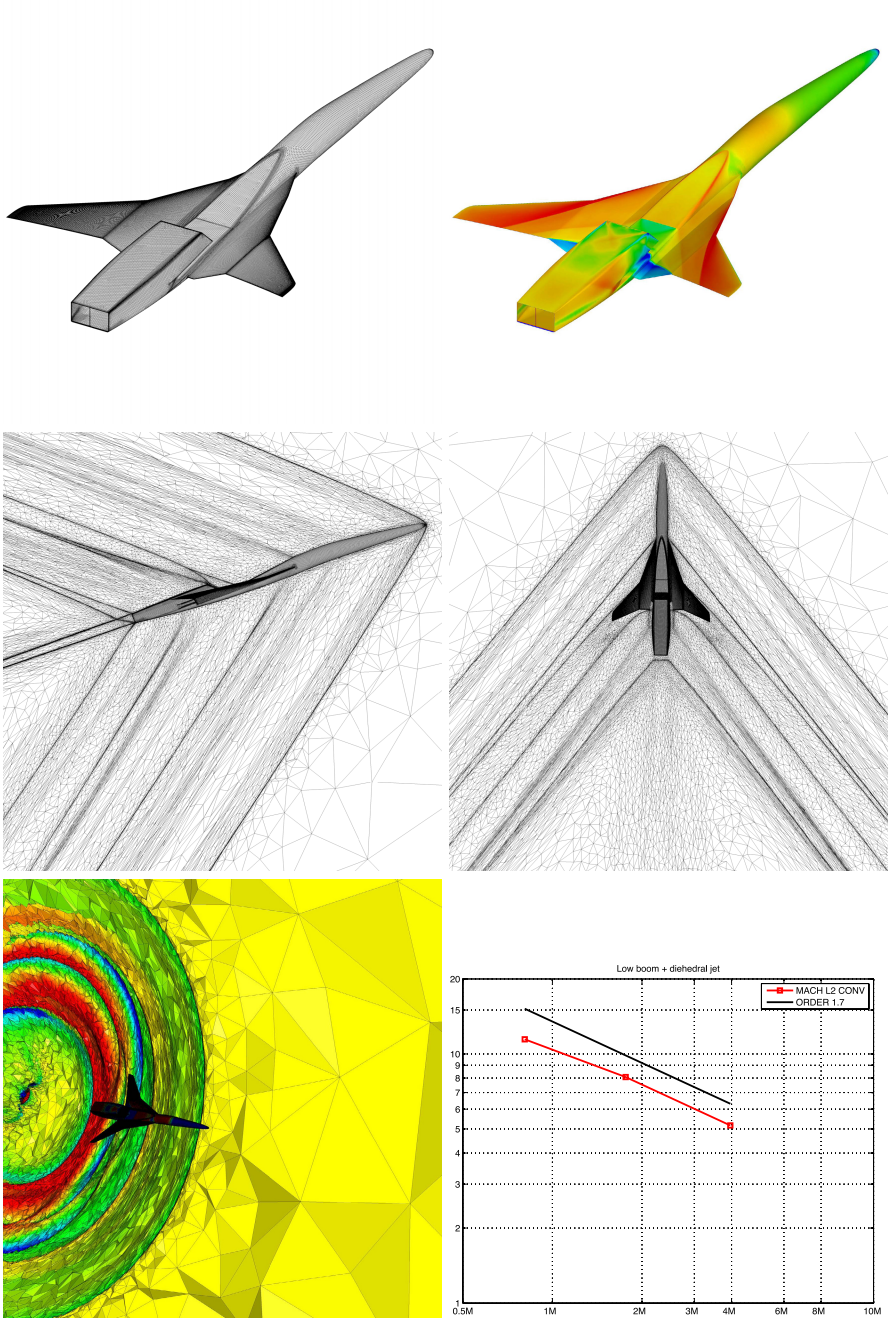


**Fig. 7.** Supersonic flow around a lowboom jet. From top to bottom, from left to right, aircraft geometry, Mach iso-values on the geometry, final anisotropic mesh in the symmetry plane and below the aircraft, Mach iso-values in a plane 50m behind the aircraft and order of convergence of the Mach number.

*Transonic flow around a Falcon.* The Falcon jet geometry is depicted in Figure 6 (top left). The aircraft is flying at Mach number 0.8 with an angle of attack of 3 degrees. The computational domain is a cylinder of radius 250m and of length 700m. As the aircraft is flying at a transonic speed, the flow is composed of both shocks and smooth vortices. These phenomena have different magnitudes and mathematical properties. Across a shock, most variables become discontinuous whereas a vortex corresponds to a smooth variation of the variables while having a very small amplitude. These features are exemplified in Figure 6 (top right). An extraction of the pressure across the wing extrados where a shock occurs (green curve) is superposed to the pressure variation in the wake across a vortex located 400m behind the aircraft (red curve). The amplitude of the vortex is less than 2% of the amplitude of the shock. Moreover, the smoothness property of the vortex is a supplementary difficulty as its derivatives involved in our estimate are also smooth. Consequently, vortices are difficult to detect and it is hard not to diffuse them. Detecting and preserving these vortices is still a challenge in the field of CFD. We show that the multi-scale approach detects these two phenomena, *i.e.,* the shocks on the wing, Figure 6 (middle) along with the vortices behind the aircraft, Figures 6 (bottom). The final anisotropic mesh depicted in Figure 6 is composed of 2 025 231 vertices and 11 860 697 tetrahedra providing a mean anisotropic ratio of 177 and a mean anisotropic quotient of 1 639. This example illustrates two main features of multi-scale anisotropic mesh adaptation: the accurate capturing of the shocks on the wings and the drastic reduction of the solver diffusion that allows us to still capture vortices 500m behind the Falcon.

*Supersonic flow around a lowboom jet.* The aircraft geometry is depicted in Figure 7 (top left). Its length is $L = 42$ meters and it has a wing span of 20 meters. The surface mesh accuracy varies between 0.2 millimeters and 12

**Table 1.** Supersonic flow around a lowboom jet: anisotropic ratios and quotients histograms for the final adapted mesh. For each interval, the number of tetrahedra is given with the corresponding percentage.

| Anisotropic ratio | | |
|---|---|---|
| $1 \leq$ ratio $\leq 2$ | 38 740 | 0.07 % |
| $2 \leq$ ratio $\leq 3$ | 175 929 | 0.33 % |
| $3 \leq$ ratio $\leq 4$ | 274 955 | 0.51 % |
| $4 \leq$ ratio $\leq 5$ | 328 501 | 0.61 % |
| $5 \leq$ ratio $\leq 10$ | 1 55 4625 | 2.89 % |
| $10 \leq$ ratio $\leq 50$ | 6 620 533 | 12.29 % |
| $50 \leq$ ratio $\leq 10^2$ | 5 983 308 | 11.10 % |
| $10^2 \leq$ ratio $\leq 10^3$ | 34 830 344 | 64.64 % |
| $10^3 \leq$ ratio $\leq 10^4$ | 4 077 796 | 7.57 % |
| $10^4 \leq$ ratio $\leq 10^5$ | 131 | 0.00 % |
| $10^5 \leq$ ratio $\leq$ | 1 | 0.00 % |

| Anisotropic quotient | | |
|---|---|---|
| $1 \leq$ quo $\leq 2$ | 10 042 | 0.02 % |
| $2 \leq$ quo $\leq 3$ | 50 171 | 0.09 % |
| $3 \leq$ quo $\leq 4$ | 81 027 | 0.15 % |
| $4 \leq$ quo $\leq 5$ | 100 385 | 0.19 % |
| $5 \leq$ quo $\leq 10$ | 526 474 | 0.98 % |
| $10 \leq$ quo $\leq 50$ | 1 989 374 | 3.69 % |
| $50 \leq$ quo $\leq 10^2$ | 1 204 384 | 2.24 % |
| $10^2 \leq$ quo $\leq 10^3$ | 7 408 172 | 13.75 % |
| $10^3 \leq$ quo $\leq 10^4$ | 14 595 766 | 27.09 % |
| $10^4 \leq$ quo $\leq 10^5$ | 20 999 034 | 38.97 % |
| $10^5 \leq$ quo $\leq 10^6$ | 6 790 336 | 12.60 % |
| $10^6 \leq$ quo | 129 698 | 0.24 % |

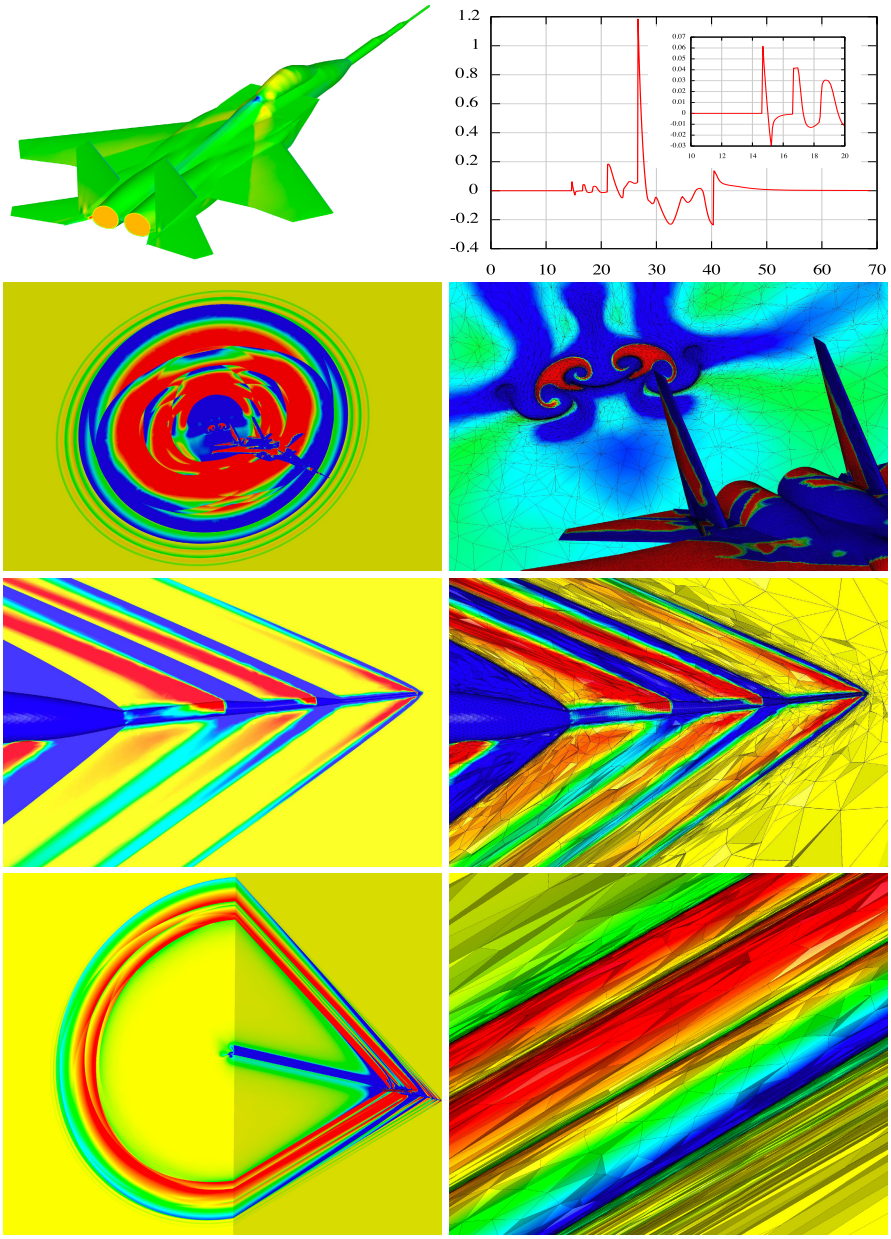


**Fig. 8.** F15 fighter equipped with the Quiet Spike. From top to bottom, from left to right, F15 geometry and Mach iso-values, pressure distribution 2m below the aircraft, Mach iso-values behind the aircraft, vortices details behind the F15, Mach iso-values near the Spike, anisotropic mesh near the spike, Mach iso-values in a 100m wide box and accuracy of the mesh 100m below the aircraft.

centimeters. This already represents a size variation of five orders of magnitude with respect to the aircraft size, and this only for the surface mesh. The computational domain is a cylinder of 2.25 kilometers length and 1.5 kilometers diameter. This represents a scale factor of $10^7$ if the size of the domain is compared to the maximal accuracy of the low boom jet surface mesh. The final anisotropic mesh is composed of 9 083 53 vertices and 53 884 863 tetrahedra. This accuracy allows us to capture all the shocks emitted by the aircraft up to a distance of 16 times the length of the aircraft (almost 750m), Figure 7 (middle). The level of anisotropy reached in this simulation is quite impressive. Indeed, the mean anisotropic quotient is almost 50 000 which is very high. Detailed histograms are given in Table 1. Besides this high level of anisotropy, this simulation demonstrates the good correlation with the theory (10) as a 1.7 order of convergence is numerically verified on the sequence of adaptive meshes, see Figure 7 (bottom right). As in the previous examples, the multi-scale strategy reduces the flow solver dissipation that allows us to capture all solution scales while maintaining a high level of anisotropy.

*F15 fighter equipped with the Quiet Spike.* We consider in this example the accurate prediction of the mid-field pressure signature of the F15 fighter equipped with the Quiet Spike concept [12] during a supersonic flight. The aircraft is flying at Mach 1.8 with an angle of attack of 0 degree. This complex geometry is shown in Figure 8 (top left). This concept was devised to soften the sonic boom by splitting the initial strong bow shock in several shocks of smaller amplitudes. The different scales of the pressure distribution are depicted in Figure 8 (top right). The Quiet Spike is composed of three cones linked by cylinders of increasing radius. The smallest cylinder has a radius of 5cm while the greatest one has a radius of 20cm. These sizes must be compared to the aircraft length 19.3m and wing-span 13m. The scale variations of the geometry give a first idea of the complexity of this simulation.

**Table 2.** F15 fighter equipped with the Quiet Spike: anisotropic ratios and quotients histograms for the final adapted mesh. For each interval, the number of tetrahedra is given with the corresponding percentage.

| Anisotropic ratio | | |
|---|---|---|
| $1 \leq$ ratio $\leq 2$ | 515 23 | 0.09 % |
| $2 \leq$ ratio $\leq 3$ | 245 783 | 0.41 % |
| $3 \leq$ ratio $\leq 4$ | 373 769 | 0.62 % |
| $4 \leq$ ratio $\leq 5$ | 429 601 | 0.71 % |
| $5 \leq$ ratio $\leq 10$ | 2 365 083 | 3.92 % |
| $10 \leq$ ratio $\leq 50$ | 17 823 972 | 29.57 % |
| $50 \leq$ ratio $\leq 10^2$ | 15 172 581 | 25.17 % |
| $10^2 \leq$ ratio $\leq 10^3$ | 23 780 955 | 39.45 % |
| $10^3 \leq$ ratio $\leq$ | 37 332 | 0.06 % |

| Anisotropic quotient | | |
|---|---|---|
| $1 \leq$ quo $\leq 2$ | 13 096 | 0.02 % |
| $2 \leq$ quo $\leq 3$ | 645 48 | 0.11 % |
| $3 \leq$ quo $\leq 4$ | 102 693 | 0.17 % |
| $4 \leq$ quo $\leq 5$ | 118 128 | 0.20 % |
| $5 \leq$ quo $\leq 10$ | 598 219 | 0.99 % |
| $10 \leq$ quo $\leq 50$ | 3 176 207 | 5.27 % |
| $50 \leq$ quo $\leq 10^2$ | 2 676 990 | 4.44 % |
| $10^2 \leq$ quo $\leq 10^3$ | 17 153 343 | 28.46 % |
| $10^3 \leq$ quo $\leq 10^4$ | 26 329 992 | 43.68 % |
| $10^4 \leq$ quo $\leq 10^5$ | 9 808 547 | 16.27 % |
| $10^6 \leq$ quo | 238 843 | 0.40 % |

In the literature, this simulation is currently envisaged in a 2-stage process by coupling a structured solver with an unstructured one [12] which provides an accurate pressure field far below the aircraft with a limit at 70m. Here, the final adapted meshes is composed of 10 050 445 vertices and 60 280 606 tetrahedra featuring a mean anisotropic ratio of 110 and a mean anisotropic quotient of 6 400. This mesh comes up with an accurate signature 120m below the aircraft while using only unstructured meshes. Detailed histograms for anisotropic quotients and ratios are reported in Table 2.

## Conclusion

A multi-scale mesh adaptation strategy has been introduced in this paper. It involves theoretical developments demonstrating that a field of metric tensors completely models discrete meshes and that the notion of interpolation error is well-defined in this continuous framework. Contrary to discrete classical approaches, the interpolation error can be computed analytically without any *a priori* hypothesis on the mesh. The optimal mesh minimizing the $\mathbf{L}^p$ norm of the interpolation error is then derived as a global optimum by a calculus of variations. The algorithm to derive a discrete optimal mesh is based on the definition of unit-mesh. Consequently, this method can be used with any metric-based mesh generators.

From a practical point a view, this approach automatically obtains adapted meshes with high level of anisotropy for realistic simulations. Optimal local Hessian normalization is set automatically and depends only on the choice of the norm. Prescribing a minimal size is no more necessary. In addition, numerical results show that all the scales of the solution are captured and refined when using an $\mathbf{L}^p$ norm error control: shocks, shear layers, ... There is no need to fix some parameters as in previous Hessian normalizations. During a simulation, verifying that a second order of convergence is reached as predicted by the theory gives a first assessment of the computations. Finally, the convergence to the most accurate solution is done in a natural way by increasing the complexity $N$ which is, along with the $\mathbf{L}^p$ norm, the only parameter to set prior to a simulation.

## References

1. Alauzet, F., Loseille, A.: High order sonic boom modeling by adaptive methods. RR-6845, INRIA (2009)
2. Babuska, I., Aziz, A.K.: On the angle condition in the finite element method. SIAM J. Numer. Anal. 13, 214–226 (1976)
3. Bottasso, C.L.: Anisotropic mesh adaption by metric-driven optimization. Int. J. Numer. Meth. Engng. 60, 597–639 (2004)
4. Castro-Díaz, M.J., Hecht, F., Mohammadi, B., Pironneau, O.: Anisotropic unstructured mesh adaptation for flow simulations. Int. J. Numer. Meth. Fluids 25, 475–491 (1997)

5. Chen, L., Sun, P., Xu, J.: Optimal anisotropic simplicial meshes for minimizing interpolation errors in $L^p$-norm. Math. Comp. 76(257), 179–204 (2007)
6. Coupez, T.: Génération de maillages et adaptation de maillage par optimisation locale. Revue Européenne des Éléments Finis 9, 403–423 (2000)
7. Dobrzynski, C., Frey, P.J.: Anisotropic delaunay mesh adaptation for unsteady simulations. In: Proc. of 17th Int. Meshing Rountable, pp. 177–194. Springer, Heidelberg (2008)
8. Formaggia, L., Perotto, S.: New anisotropic a prioiri error estimate. Numer. Math. 89, 641–667 (2001)
9. Frey, P.J., Alauzet, F.: Anisotropic mesh adaptation for CFD computations. Comput. Meth. Appl. Mech. Engrg. 194(48-49), 5068–5082 (2005)
10. Frey, P.J., George, P.-L.: Mesh generation. Application to finite elements, 2nd edn. ISTE Ltd and John Wiley & Sons (2008)
11. George, P.-L.: Gamhic3d, a fully automatic adaptive mesh generation method in three dimensions. Technical Note, INRIA (2001)
12. Howe, D.C., Waithe, K.A., Haering, E.A.: Quiet spike near field flight test pressure measurement with computational fluid dynamics comparisons. AIAA Paper, 2008-128 (2008)
13. Huang, W.: Metric tensors for anisotropic mesh generation. J. Comp. Phys. 204, 633–665 (2005)
14. Lagüe, J.-F., Hecht, F.: Optimal mesh for $P_1$ interpolation in $H^1$ semi-norm. In: Proc. of 15th Meshing Rountable, pp. 259–270. Springer, Heidelberg (2006)
15. Löhner, R.: Three-dimensional fluid-structure interaction using a finite element solver and adaptive remeshing. Computing Systems in Engineering 1(2-4), 257–272 (1990)
16. Loseille, A.: Adaptation de maillage 3D anisotrope multi-échelles et ciblé à une fonctionnelle. Application à la prédiction haute-fidélité du bang sonique. PhD thesis, Université Pierre et Marie Curie, Paris VI, Paris, France (2008)
17. Loseille, A., Alauzet, F.: Continuous mesh model and well-posed continuous interpolation error estimation. RR-6846, INRIA (2009)
18. Pain, C.C., Umpleby, A.P., de Oliveira, C.R.E., Goddard, A.J.H.: Tetrahedral mesh optimisation and adaptivity for steady-state and transient finite element calculations. Comput. Meth. Appl. Mech. Engrg. 190, 3771–3796 (2001)
19. Tam, A., Ait-Ali-Yahia, D., Robichaud, M.P., Moore, M., Kozel, V., Habashi, W.G.: Anisotropic mesh adaptation for 3D flows on structured and unstructured grids. Comput. Meth. Appl. Mech. Engrg. 189, 1205–1230 (2000)